ADVANCED MATERIALS

Supporting Information

for *Adv. Mater.*, DOI: 10.1002/adma.201605800

Atomimetic Mechanical Structures with Nonlinear Topological Domain Evolution Kinetics

*Michael J. Frazier and Dennis M. Kochmann**

Supporting Information for

Atomimetic Mechanical Structures with Nonlinear Topological Domain Evolution Kinetics

In these supplementary sections, we provide the complete derivations of equations appearing in the main article as well as further details and additional results from simulations.

1 The Local Energy Potential

Absent the influence of a coercive gravitational field, the on-site potential ψ of a single cylinder in the periodic network is determined by two elementary mechanical components: a torsional spring of stiffness k_0 located about the rotation axis of the cylinder, and an axial spring of stiffness k_B fixed at one end to the cylinder and the other end to an adjustable plane (ceiling) parallel to the cylinder foundation (and thus perpendicular to the rotation axis). The energy contribution of the torsional spring is simply

$$\psi_0(\varphi) = k_0(\varphi - \varphi_0)^2/2, \tag{S1}$$

so that the zero-energy ground state is $\varphi_0 = 0$.

The bistable energy potential is effected by the axial spring connection to the ceiling whose energy contribution $\psi_\mathrm{B}(\varphi)$ follows with reference to the schematic in Figure S1a, where the origin of the coordinate axes is the center of the exposed circular surface of the rotating cylinder. One end of the linear spring is attached to an eccentric mass on the cylinder whose position is given by

$$\boldsymbol{r}_m = r[\cos(\varphi + \varphi_m),\, \sin(\varphi + \varphi_m),\, 0]^\mathrm{T}, \tag{S2}$$

with $r > 0$ the radial distance from the origin and the offset $\varphi_m \in [0, 2\pi)$ measured from the x-axis. Here, we choose $r = R$ and $\varphi_m = \pi$. The other end of the linear spring is attached to the ceiling at $\boldsymbol{r}_\mathrm{A} = R\boldsymbol{f}$ with $\boldsymbol{f} = [f_\mathrm{x}, f_\mathrm{y}, f_\mathrm{z}]^\mathrm{T}$, where $f_i \in \mathbb{R}$ are dimensionless scaling coefficients. The constraint $f_\mathrm{z} > 0$ prevents

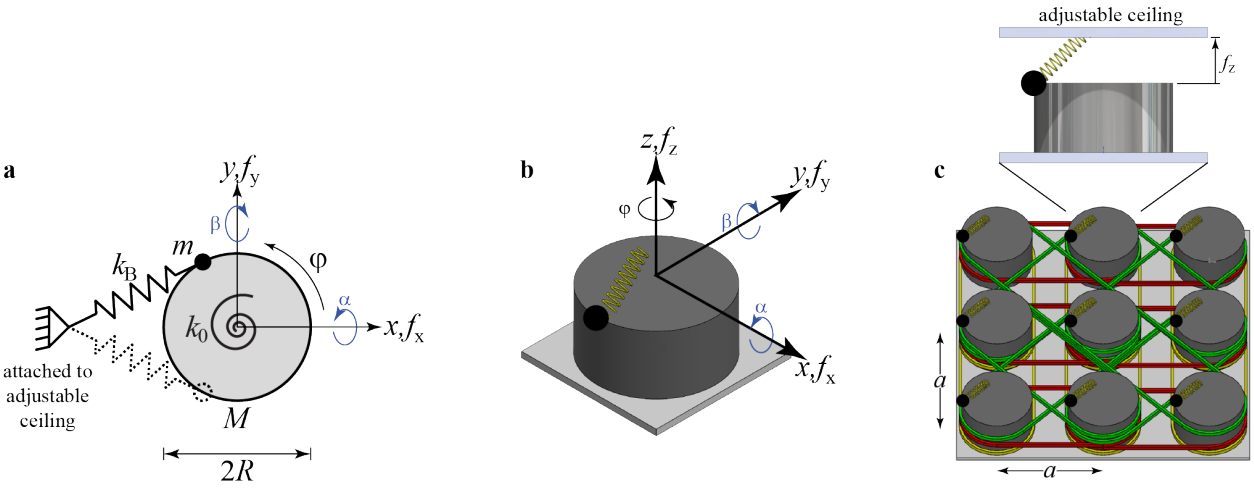

Figure S1: Atomimetic mechanical structure. a) A schematic of the rotating cylinder system as viewed from above with an axial spring of stiffness k_B responsible for multistability, a torsional spring of stiffness k_0 which renders the system bistable, and an eccentric mass m which, through the action of gravity (present when $\alpha, \beta \neq 0$), imbues a switching capacity. Damping (not shown) with viscosity coefficient η resists angular motion. b) A model of the bistable cylinder with the ceiling removed. Rotation φ is about the z-axis, positive counter-clockwise when viewed down the axis (in the negative z-direction). Positive rotations about x- and y-axes are similarly defined, respectively, for α and β. c) Connecting a number of such bistable cylinders with elastic bands forms the bistable periodic network.

contact between the ceiling and cylinder. Thus, the deformed length of the spring is given by $\ell = |\boldsymbol{L}|$ with the distance vector $\boldsymbol{L} = \boldsymbol{r}_\mathrm{A} - \boldsymbol{r}_m$, or

$$\ell(\varphi, \boldsymbol{f}) = R\sqrt{1 + |\boldsymbol{f}|^2 + 2(f_\mathrm{x}\cos\varphi + f_\mathrm{y}\sin\varphi)}. \tag{S3}$$

If we define $\ell_0 = \ell(\varphi_\mathrm{N}, \boldsymbol{f}_\mathrm{N})$ as the natural (unstretched) spring length, then the spring energy becomes

$$\psi_\mathrm{B}(\varphi, \boldsymbol{f}) = \frac{k_\mathrm{B}}{2}\big[\ell(\varphi, \boldsymbol{f}) - \ell_0\big]^2. \tag{S4}$$

The final contribution to the nonlinear on-site potential ψ, one which enables domain switching due to an applied field, is the gravitational contribution emerging from the eccentricity of mass m. Angles α and β, respectively, measure the rotation of the cylinder assembly about the x- and y-axes (and we write $\boldsymbol{\theta} = \{\alpha, \beta\}$ for short) (see Figure **S1**b). With gravitation acting along the negative z-axis and the default $\alpha = \beta = 0$, the potential energy contribution of a single mass rotated by φ reads

$$\psi_\mathrm{g}(\varphi, \boldsymbol{\theta}) = -mgh(\varphi, \boldsymbol{\theta}) \qquad \text{with} \qquad h(\varphi, \boldsymbol{\theta}) = R(\sin\alpha\sin\varphi - \cos\alpha\sin\beta\cos\varphi). \tag{S5}$$

The zero-level is chosen such that $\psi_\mathrm{g} = 0$ when $\alpha = \beta = \varphi = 0$.

In total, with tuning parameters $\boldsymbol{\theta} = \{\alpha, \beta\}$ and $\boldsymbol{f} = \{f_\mathrm{x}, f_\mathrm{y}, f_\mathrm{z}\}$, the on-site energy potential

$$\psi(\varphi, \boldsymbol{\theta}, \boldsymbol{f}) = \psi_0(\varphi) + \psi_\mathrm{B}(\varphi, \boldsymbol{f}) + \psi_\mathrm{g}(\varphi, \boldsymbol{\theta}) \tag{S6}$$

is the sum of mechanical and gravitational influences acting on an individual element.

In the following we exploit $\boldsymbol{f}$ to transition between a single- and double-well potential in analogy to the Landau-Devonshire energy of second-order phase transformations [1, 2, 3]. Specifically, we fix $f_\mathrm{y} = 0$ and $f_\mathrm{z} = f_\mathrm{Nz} > 0$ and vary f_x. A convex single-well potential results from $f_\mathrm{x} = 0$ and produces the (unpolar) "high-temperature" phase with $\varphi = 0$ (see Figure **S2**a). Increasing f_x above $f_\mathrm{c} \approx 1.78$ turns ψ into a double-well potential (see Figure **S2**b), analogous to a second-order transition, corresponding to two (polar) equilibrium phases with stable equilibria at $\pm\varphi$. The critical threshold f_c is found by considering the curvature of the energy landscape, or the roots of $\psi''(\varphi = 0, \boldsymbol{\theta} = \boldsymbol{0}, f_\mathrm{c}) = 0$, i.e., the instant at which there is a change in stability. Explicitly,

$$f_\mathrm{c} k_\mathrm{B} R^2 \left(\frac{\sqrt{f_\mathrm{xN}^2 + 2f_\mathrm{xN}\cos\varphi_\mathrm{N} + f_\mathrm{z}^2 + 1}}{\sqrt{(f_\mathrm{c}+1)^2 + f_\mathrm{z}^2}} - 1 \right) + k_0 = 0, \tag{S7}$$

which may be numerically solved for f_c. In particular, the main article uses $\boldsymbol{f}_\mathrm{N} = \{-2, 0, 1/10\}$, $\varphi_\mathrm{N} = 85°$, and $k_\mathrm{B}R^2/k_0 = 2.5$, so that $f_\mathrm{c} \approx 1.78$.

For ferroelectrics which undergo a second-order phase transformation, the Landau-Ginzburg polynomial expansion of the free energy density F may be expressed (for simplicity written in 1D) as follows [4]:

$$F = C_0 + C_1(T - T_0)p^2 + C_2 p^4 + O(p^5), \tag{S8}$$

where C_0 is the free energy density of the paraelectric phase with vanishing electric field, and p is the polarization. The coefficients C_1 and C_2 are, in general, positive, temperature- and pressure-dependent. The crystal and Curie temperatures are, respectively, T and T_0. Neglecting higher-order terms, stability requirements, i.e., $\mathrm{d}F/\,\mathrm{d}p = 0$ and $\mathrm{d}^2F/\,\mathrm{d}p^2 > 0$, yield the following prediction for the spontaneous polarization if $T \leq T_0$:

$$p^2 = -\frac{C_1(T - T_0)}{2C_2}. \tag{S9}$$

Analogously, in the absence of gravitational effects, the symmetric on-site potential energy of our bistable cylinder may be expanded in a Taylor series about $\{\varphi, f_x\} = \{0, f_\mathrm{c}\}$ as

$$\psi = \sum_{i=0}^{\infty}\sum_{j=0}^{\infty} C_{ij}(f_\mathrm{x} - f_\mathrm{c})^i \varphi^{2j}. \tag{S10}$$

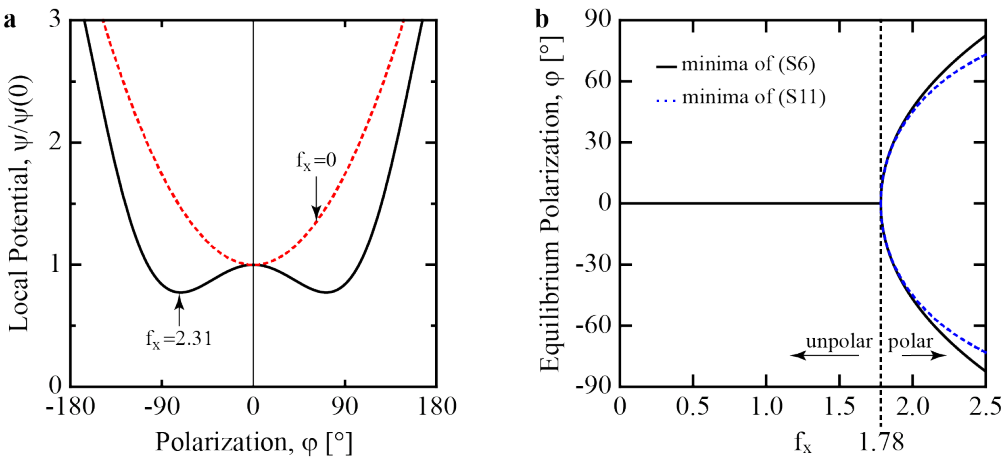

Figure S2: Phase transformation. a) The mechanical structure displays a phase transformation as the action of the axial spring is nullified by $f_x \to 0$, removing the characteristic bistability. b) This causes the two equilibrium polarizations to coalesce into one.

As $f_x \to f_c$ from above, the leading-order terms dominate and Equation (S10) may be approximated as

$$\psi \approx C_{1,1} + C_{2,1}(f_x - f_c) + [C_{1,2} + C_{2,2}(f_x - f_c)]\varphi^2 + [C_{1,3} + C_{2,3}(f_x - f_c)]\varphi^4. \tag{S11}$$

Naturally, we employ the same material parameters as the main text, which yields specific values of constants $C_{i,j}$. Note that $C_{1,2} = 0$, $C_{2,2} < 0$ while all other $C_{i,j} > 0$. Using the analogous requirements $\mathrm{d}\psi/\,\mathrm{d}\varphi = 0$ and $\mathrm{d}^2\psi/\,\mathrm{d}\varphi^2 > 0$, we solve for the spontaneous polarization $\varphi = \varphi(f_x)$ for $f_x \geq f_c$ and plot the result in Figure **S2**b (shown are solutions obtained from both exact and truncated potentials, showing significant deviations only far from f_c). Analogous to Equation (S9), this results for $f_x \geq f_c$ in the equilibrium polarizations given by

$$\varphi^2 = -\frac{C_{2,2}(f_x - f_c)}{2[C_{1,3} + C_{2,3}(f_x - f_c)]} \approx -\frac{C_{2,2}(f_x - f_c)}{2C_{1,3}} + O[(f_x - f_c)^2]. \tag{S12}$$

Comparison with Equation (S9) shows that the leading-order scaling of the mechanical metamaterial polarization φ and the ferroelectric polarization p scale indeed equally with T and f_x, respectively; i.e., both systems display the same critical exponent of $1/2$ as $\varphi_{1,2} \propto (f_x - f_c)^{1/2}$.

For ferroelectrics/magnets, the polarized state results from an asymmetry in the crystal structure which vanishes above the Curie temperature where the only stable equilibrium is the unpolarized state of fixed energy. Below this critical temperature, the unpolarized state becomes an unstable equilibrium. Although not qualitatively important to the results, the same feature may be reproduced in the rotating cylinder by choosing a specific f_x which is found by equating $\psi(f_x) = \psi(f_x = 0)$ at $\varphi = 0$ in the level orientation ($\boldsymbol{\theta} = \mathbf{0}$), that is,

$$f_x + \frac{f_x^2}{2} - \left(\sqrt{(1+f_x)^2 + f_z^2} - \sqrt{1+f_z^2}\right)\sqrt{1 + f_z^2 + f_{xN}^2 + 2f_{xN}\cos\varphi_N} = 0. \tag{S13}$$

This yields four solutions:

$$f_x = \begin{cases} 0, \\ -2, \\ -1 \pm 2\sqrt{\frac{5}{4} + \delta - \sqrt{1+f_z^2}\sqrt{1+\delta}}, \end{cases} \tag{S14}$$

with $\delta = f_z^2 + f_{xN}^2 + 2f_{xN}\cos\varphi_N$.

2 Discrete Network and Continuum Limit

Utilizing the above bistable element, the network of Figure 1e results from the arrangement of many such elements in a two-dimensional lattice with elastic bands connecting and transferring energy between neighboring elements, see Figure S1c. Starting with the discrete Hamiltonian, Equation (1) in the article, and

assuming velocity-proportional damping $\eta > 0$, the governing equation of a cylinder at position $\boldsymbol{x}$ and connected to n neighbors at positions $\boldsymbol{x} + \Delta\boldsymbol{x}_\gamma$ ($\gamma = 1, \dots, n$) via elastic bands of stiffness k_γ is

$$I\ddot{\varphi}(\boldsymbol{x}) + \eta\,\dot{\varphi}(\boldsymbol{x}) + \psi'\left[\varphi(\boldsymbol{x}), \boldsymbol{\theta}, \boldsymbol{f}\right] = R^2 \sum_{\gamma=1}^{n} k_\gamma \left[\varphi(\boldsymbol{x} + \Delta\boldsymbol{x}_\gamma) - \varphi(\boldsymbol{x})\right], \tag{S15}$$

where $\psi(\varphi, \boldsymbol{\theta}, \boldsymbol{f})$ is the nonlinear on-site potential of Equation (S6).

We apply methods of homogenization to pass to the continuum limit of a very large network of rotating disks, ultimately described by a continuous polarization field $\varphi(\boldsymbol{x})$. This is the abstraction process analogous to modeling atomistic systems by mesoscale phase field theories, ferroelectric ceramics being a prominent example [5, 6, 7]. Starting with Equation (S15), we define $\Delta\boldsymbol{x}_\gamma = a\,\boldsymbol{e}^\gamma$ where a is the side length of the discrete unit cell (i.e., the characteristic spacing between disks in the lattice), and $\boldsymbol{e}^\gamma$ is the corresponding (not normalized) distance vector. A Taylor expansion of $\varphi(\boldsymbol{x} + \Delta\boldsymbol{x}_\gamma)$ (assuming sufficient smoothness for differentiability and using index notation with summation convention) leads to

$$\varphi(\boldsymbol{x} + \Delta\boldsymbol{x}_\gamma) = \varphi(\boldsymbol{x}) + a\varphi_{,i}(\boldsymbol{x})e_i^\gamma + \frac{a^2}{2}\varphi_{,ij}(\boldsymbol{x})e_i^\gamma e_j^\gamma + \frac{a^3}{6}\varphi_{,ijk}(\boldsymbol{x})e_i^\gamma e_j^\gamma e_k^\gamma + O(a^4). \tag{S16}$$

The interaction term in Equation (S15) thus becomes

$$\begin{aligned} R^2 \sum_{\gamma=1}^{n} k_\gamma \left[\varphi(\boldsymbol{x} + \Delta\boldsymbol{x}_\gamma) - \varphi(\boldsymbol{x})\right] = \\ R^2 a\varphi_{,i}(\boldsymbol{x}) \sum_{\gamma=1}^{n} k_\gamma e_i^\gamma + \frac{R^2 a^2}{2}\varphi_{,ij}(\boldsymbol{x}) \sum_{\gamma=1}^{n} k_\gamma e_i^\gamma e_j^\gamma \\ + \frac{R^2 a^3}{6}\varphi_{,ijk}(\boldsymbol{x}) \sum_{\gamma=1}^{n} k_\gamma e_i^\gamma e_j^\gamma e_k^\gamma + O(a_\gamma^4). \end{aligned} \tag{S17}$$

Notice that for centro-symmetric lattices the leading-order term in (S17) vanishes since centro-symmetry [8] implies $\sum_{\gamma=1}^{n} k_\gamma \boldsymbol{e}^\gamma = \boldsymbol{0}$.

Before passing to the continuum limit as $a \to 0$, it is essential that the system parameters obey the correct scaling, so that the continuum governing equation and associated solutions remain finite in the limit. This requires that the continuum inertial density ρ, viscosity ν, and stiffness values c_γ satisfy

$$\frac{I}{a^2} = \rho \sim O(1), \quad \frac{\eta}{a^2} = \nu \sim O(1), \quad \frac{k_\gamma R^2 a^2}{a^2} = c_\gamma \sim O(1), \tag{S18}$$

which can easily be obtained by scaling arguments of the total kinetic and potential energy and the total dissipation potential [9]. Insertion into (S15) along with (S17) for centro-symmetric lattices shows that all terms of order $O(a^3)$ and higher vanish in the continuum limit (i.e., as $a \to 0$). Therefore, the continuum limit of a centro-symmetric lattice is governed by

$$\rho\,\ddot{\varphi}(\boldsymbol{x}) + \nu\,\dot{\varphi}(\boldsymbol{x}) - \frac{1}{2}\varphi_{,ij} \sum_{\gamma=1}^{n} c_\gamma e_i^\gamma e_j^\gamma + \psi'\big(\varphi(\boldsymbol{x}), \boldsymbol{\theta}, \boldsymbol{f}\big) = 0. \tag{S19}$$

Introducing the abbreviation

$$\kappa_{ij} = \frac{1}{2} \sum_{\gamma=1}^{n} c_\gamma e_i^\gamma e_j^\gamma \tag{S20}$$

finally leads to Equation (3) in the article, viz.

$$\rho\,\ddot{\varphi}(\boldsymbol{x}) + \nu\,\dot{\varphi}(\boldsymbol{x}) = \kappa_{ij}\frac{\partial^2 \varphi}{\partial x_i \partial x_j} - \psi'\big(\varphi(\boldsymbol{x}), \boldsymbol{\theta}, \boldsymbol{f}\big). \tag{S21}$$

In case of significant damping (e.g., through friction) we have $|\rho\,\ddot{\varphi}| \ll |\nu\,\dot{\varphi}|$ so that (S21) reduces to the Allen-Cahn equation [10, 11]. Of course, damping in the system can be arbitrarily complex, so the linear approximation chosen here is only a leading-order approximation which, however, worked excellently for our experimentally investigated 1D bistable networks [12, 13]. Linear gradient flow is also the most common kinetic model used in phase field description [5, 6, 7].

3 Energy Transport and Domain Wall Motion in the Discrete Network

We recently reported a universal scaling law for the energy transported by 1D transition waves in periodic networks of bistable elements [9]. As shown in the following, those results also apply to planar transition fronts propagating in the 2D discrete system discussed here with important implications on width, speed, and energy of moving domain walls.

We seek a traveling plane-wave solution $\varphi(\boldsymbol{x},t)=\varphi(\hat{\boldsymbol{e}}\cdot\boldsymbol{x}-vt)$, with $\hat{\boldsymbol{e}}$ the unit vector in the direction of wave propagation and v the wave speed. Following the abbreviation $z=\hat{\boldsymbol{e}}\cdot\boldsymbol{x}-vt$ and assuming sufficient smoothness of solutions, (S15) becomes

$$v^2 I\varphi_{,zz}-v\eta\varphi_{,z}+\psi'(\varphi,\boldsymbol{\theta},\boldsymbol{f})=R^2\sum_{\gamma=1}^{n}k_\gamma\big[\varphi(z+\hat{\boldsymbol{e}}\cdot\Delta\boldsymbol{x}_\gamma)-\varphi(z)\big]. \tag{S22}$$

Multiplication by $\varphi_{,z}$ and integration over the real axis (which may be interpreted as integration along an infinite path perpendicular to the transition front) leads to

$$\begin{aligned}\int_{-\infty}^{\infty}\big[v^2 I\varphi_{,zz}-v\eta\varphi_{,z}+\psi'(\varphi,\boldsymbol{\theta},\boldsymbol{f})\big]\varphi_{,z}\,\mathrm{d}z=\\ R^2\sum_{\gamma=1}^{n}k_\gamma\int_{-\infty}^{\infty}\big[\varphi(z+\hat{\boldsymbol{e}}\cdot\Delta\boldsymbol{x}_\gamma)-\varphi(z)\big]\varphi_{,z}\,\mathrm{d}z.\end{aligned} \tag{S23}$$

While not analytically solvable in general, the initial and boundary conditions admit the following assumptions. The dissipative/diffusive nature of the system ensures that, far from the interface region (i.e., for $|z|\to\infty$) the polarization φ assumes a constant, steady value (φ_+ or φ_-) so that $\varphi(z+\hat{\boldsymbol{e}}\cdot\Delta\boldsymbol{x}_\gamma)-\varphi(z)\to 0$. This can be shown to make the interaction term vanish [9]. In addition, a similar argument can be applied to the inertial term. Consequently, the inertial term also vanishes and Equation (S23) reduces to

$$v\,\eta\int_{-\infty}^{\infty}\varphi_{,z}^2\,\mathrm{d}z=\int_{-\infty}^{\infty}\psi'(\varphi,\boldsymbol{\theta},\boldsymbol{f})\,\varphi_{,z}\,\mathrm{d}z. \tag{S24}$$

Since the wave front interpolates between two stable configurations, $\varphi_-=\lim_{z\to\infty}\varphi(z)$ and $\varphi_+=\lim_{z\to-\infty}\varphi(z)$, the on-site potential contribution (i.e., the right-hand side in Equation (S24)) equals $\Delta\psi=\psi(\varphi_-,\boldsymbol{\theta},\boldsymbol{f})-\psi(\varphi_+,\boldsymbol{\theta},\boldsymbol{f})$, the energy released by the transition. This gives

$$v\,\eta\int_{-\infty}^{\infty}\varphi_{,z}^2\,\mathrm{d}z=\Delta\psi, \tag{S25}$$

where — for large wave widths ($w\gg d$, with $d\propto a$ the separation between sites in the propagation direction) — the left-hand side may be interpreted as the total dissipation or the total kinetic energy per inertial density of the network. Specifically, we define $E_\mathrm{d}=\frac{v}{2}\int_{-\infty}^{\infty}\varphi_{,z}^2\,\mathrm{d}z$ which depends on the transition waveform and can be determined if the shape of the moving domain wall is known.

Alternatively, E_d can be computed from numerical simulations as the total transported kinetic energy per inertial density for the discrete lattice:

$$E_\mathrm{d}=\frac{v^2}{2}\int_{-\infty}^{\infty}\varphi_{,z}^2\mathrm{d}z\approx\frac{v^2}{2}\sum_{i=1}^{N_\ell}\varphi_{i,z}^2 d=\frac{d}{2}\sum_{i=1}^{N_\ell}\varphi_{i,t}^2, \tag{S26}$$

where N_ℓ is the number of lattice sites along the line of motion (seizing periodicity of the unit cell in numerical simulations to extend over the entire real axis). Together, (S25) and (S26) lead to the desired discrete scaling relation

$$\frac{E_\mathrm{d}}{v}\simeq\frac{\Delta\psi}{2\eta}. \tag{S27}$$

This implies that the balance between energy dissipation (proportional to E_d) and energy release $\Delta\psi$ by the transition drives a planar transition wave moving at constant speed v. This has been demonstrated

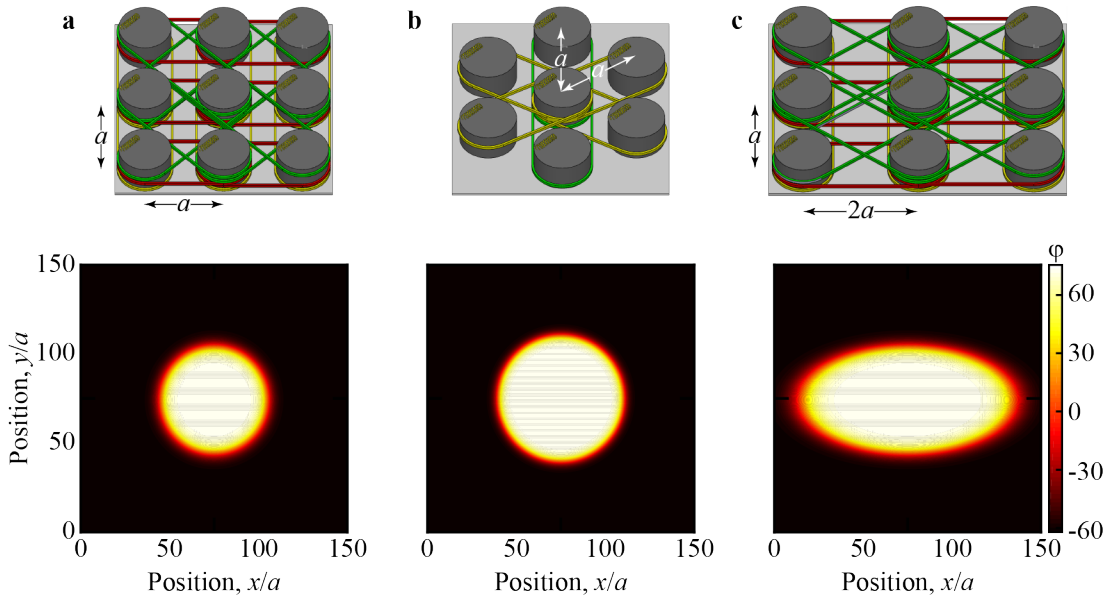

Figure S3: The domain wall energy is tuned by the connector stiffness values k_{ij} (continuous κ_{ij}), which are functions of the lattice arrangement. Isotropic lattices support mobile domain walls with direction-independent properties (i.e., speed, width) as exemplified in the a) square lattice and b) triangular lattice compared to the anisotropic c) rectangular lattice with apparent direction-dependent wave motion.

experimentally at the structural level in periodic 1D chains of elastically-coupled snapping shells [12] and snapping beams [13]. Also, transition waves travel only in the direction of decreasing energy ($v \cdot \Delta\psi \geq 0$ since $E_\mathrm{d} > 0$ by definition and $\eta > 0$ by the second law of thermodynamics). We note that the above scaling law applies even in the limit $\rho \to 0$ [9].

Let the 1D variation of the polarization perpendicular to an Ising-type domain wall be approximated by

$$\varphi(z) = \frac{\varphi_+ + \varphi_-}{2} - \frac{\varphi_+ - \varphi_-}{2} \tanh\left(\frac{z}{h}\right) \tag{S28}$$

with the origin at the center of the wall. The half-width of the domain wall is $HW = 2h$ and

$$E_\mathrm{d} = \frac{v^2}{2} \int_{-\infty}^{\infty} \varphi_{,z}^2 \mathrm{d}z = v^2 \frac{(\varphi_+ - \varphi_-)^2}{4\pi h}. \tag{S29}$$

This results in

$$\frac{v}{HW} \propto \frac{\Delta\psi}{\eta\,(\varphi_+ - \varphi_-)^2}. \tag{S30}$$

Domain boundaries are a common feature of multistable systems. For an asymmetric potential, domain wall motion is driven by the potential difference $\Delta\psi = \psi_+ - \psi_-$ between domains. For different mechanical networks, Figure S3 demonstrates radially expanding transition waves, whose wave profile and speed depend on the lattice spacing and on the elastic connections, specifically, k_γ in Equation (S15). Accordingly, the three depicted example realizations produce isotropic or anisotropic waves propagating at a direction-dependent speed, thus demonstrating the tunability of the system.

4 Interface Motion in the Phase Field Model

The kinetics of phase separation, e.g., in metal alloys [10] or of domain wall motion in ferroelectric ceramics [5, 6, 7] are often described by the Allen-Cahn equation

$$\dot{\epsilon} = \nabla \cdot (\boldsymbol{P}\, \nabla\epsilon) - Q\, \psi'(\epsilon), \tag{S31}$$

where $\psi'(\epsilon)$ is a multi-stable potential in the order parameter ϵ. $\boldsymbol{P}$ has dimensions of a diffusion tensor, and Q is a kinetic coefficient. When $|\rho\,\ddot{\varphi}| \ll |\nu\,\dot{\varphi}|$, our periodic mechanical system, described by (S21), is governed by the same equation with $\epsilon \equiv \varphi$, $P_{ij} = \kappa_{ij}/\nu = \text{const.}$, and $Q = 1/\nu$.

When the Allen-Cahn model is used to describe interface motion with isotropic interface energy (i.e., $\boldsymbol{P} = P\,\boldsymbol{I}$), we may assume the profile of the wave front remains approximately constant along the interface, so we can expand the Laplacian as

$$\nabla^2\epsilon = \epsilon_{,rr} - \varsigma\epsilon_{,r} \tag{S32}$$

where ς is the local curvature ($R_c = 1/\varsigma$, the radius of curvature), and r is the distance in the direction normal to the boundary, $\hat{\mathbf{n}}$. We adopt the convention $\varsigma > 0$ for boundaries bending toward $\hat{\mathbf{n}}$ in the direction of the gradient. Inserting (S32) into (S31) gives

$$\dot{\epsilon} = P\big[\epsilon_{,rr} - \varsigma\epsilon_{,r}\big] - Q\psi'(\epsilon) = 0. \tag{S33}$$

In addition, if the curvature is small compared to the interface thickness (i.e., $R_c \gg w$), then [11] $Q\psi'(\epsilon) - P\epsilon_{,rr} \approx 0$, reducing (S33) to

$$\dot{\epsilon} + P\varsigma\epsilon_{,r} = 0 \tag{S34}$$

giving the speed of the domain wall as $v = -\dot{\epsilon}/\epsilon_{,r}$ [11].

5 Numerical Simulations

In the article, we employ a centro-symmetric structure with $k_\gamma = k$ in Equation (S15). Dividing by k_0 and introducing the characteristic time $\tau = \sqrt{I/k_0}$ produces the nondimensional equation

$$\bar{I}\varphi_{\bar{t}\bar{t}} + \bar{\eta}\,\varphi_{\bar{t}} + \bar{\psi}'(\varphi, \boldsymbol{\theta}, \boldsymbol{f}) = \bar{k}\sum_{\gamma=1}^{n}(\varphi_\gamma - \varphi)\,, \tag{S35}$$

where $\bar{t} = t/\tau$, $\bar{I} = 1$, $\bar{\eta} = \eta/k_0\tau$, $\bar{k} = kR^2/k_0$. Within the nondimensional potential $\bar{\psi}$, we have $\bar{k}_\text{B} = k_\text{B}R^2/k_0$ and $\bar{k}_\text{g} = mgR/k_0$. Specifically, in the article we used $\bar{\eta} = 67.42$, $\bar{k} = 5$, $\bar{k}_\text{B} = 5/2$, and $\bar{k}_\text{g} = 50$; the overbars are conveniently omitted.

Simulations numerically integrate the discrete equation of motion, Equation (S15), for each cylinder in the 2D network using explicit time integration [14]. For the phase transformation, domain switching, and phase separation studies, periodic boundary conditions are enforced on all edges such that $\varphi(\boldsymbol{x}_+) = \varphi(\boldsymbol{x}_-)$ for each double of periodically-paired cylinder locations $(\boldsymbol{x}_-, \boldsymbol{x}_+)$ (see Figure **S4**a). For the energy transport study, periodic boundary condition are along the two edges normal to the wave front (see Figure **S4**b). Of the remaining two edges, one is left free and the other is prescribed rotation from φ_- to φ_+. The domain sizes are given in the *Methods* section.

In demonstrating gravitationally-induced domain switching and hysteretic behavior, we initialize a $150a \times 150a$ system in the quiescent state with each site randomly assigned a polarization φ_- or φ_+. In time, a homogeneous state evolves. As the simulation advances, $\beta = 0$ is held fixed while α cycles gradually according to:

$$\alpha(\bar{t}) = \begin{cases} -\alpha_\text{c}(|1 - 5r\bar{t}| - 1) & : \bar{t} \le \frac{3}{5}\bar{t}_\text{tot} \\ \alpha_\text{c}(|1 - 5r\bar{t}| - 3) & : \frac{3}{5}\bar{t}_\text{tot} < \bar{t} \le \bar{t}_\text{tot} \end{cases}$$

where $\alpha_\text{c} > 0$ is the angle required for gravity to affect a spontaneous switch in the mean polarization. Critically, $r = 1/\bar{t}_\text{tot}$ is chosen to be small in order to minimize rate effects (e.g., residual angular momentum). Both systems with and without randomly distributed point defects (i.e., approximately 0.5% of sites with fixed in their initial polarization) are investigated. While, in the absence of defects, domain switching is a uniform process, Movie **S1** shows defects as nucleation sites for the opposite polarization (and intervening domain walls).

We consider a $150a \times 150a$ system where dissipative (we use $\bar{\eta} = 674.2$) and interaction effects dominate over inertial and discreteness effects, i.e., a system where Equation (S31) applies. For simplicity, we initialize the system with a random polarization field. However, this state is not stable and, as depicted in Figure 5c and Movie **S2**, domains of uniform polarization organize and expand by merging with those of compatible polarization or enclosing and consuming those of the opposing state. This process mimics that of diffusive phase separation in metals and necessarily requires the motion of domain boundaries.

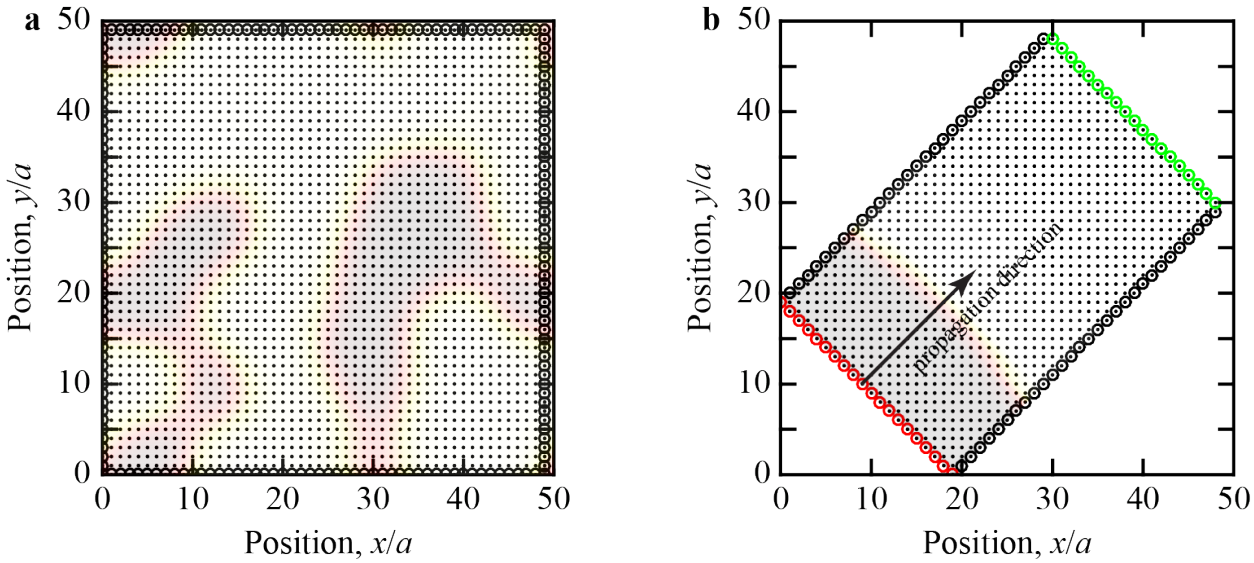

Figure S4: Periodic boundaries. a) Periodic boundary conditions (black circles) are applied at all edges in studies of phase transformation, domain switching, and phase separation. b) Studies of domain wall motion apply periodic boundary conditions only along edges perpendicular to the propagation direction with other edges being either an excitation boundary (red circles) or free boundary (green circle).

Movie S1: In the polarized state, the structure possesses two stable configurations at φ_- and φ_+ between which, through the action of a driving gravitational field (strength/direction a function of α), the system is capable of switching. For homogeneous systems, as the transition is coherent among all cylinders, the local energy landscape predicts the critical $\alpha = \alpha_c \approx 0.76°$ for switching. As depicted in this animation, the transition is non-uniform due to the presence of permanent defects. Through elastic connections k_{ij}, defects assist nearby sites in overcoming the transition energy barrier and, thus, serve as nucleation sites for the opposing polarization. This is reflected in Figure 3b,e (main text) and in this corresponding animation where defects result in premature switching (i.e., α_c is smaller than its homogeneous value).

Movie S2: In the polarized state, the structure possesses two stable configurations in φ_- and φ_+. For systems in which discreteness and inertial influences effectively vanish, phase separation (and requisite domain wall motion) proceeds according to the Allen-Cahn phase field model. In this animation (corresponding to Figure 5c), the polarization is the phase field variable. From random initial conditions, domains of opposing polarization rapidly form as smaller domains evolve quickly according to Equation (S34). As the simulation advances, domains become large and evolve more slowly.

References

[1] L. Landau, "On the theory of phase transitions (in russian)," *Zh. Eksp. Teor. Fiz.*, vol. 7, pp. 19–32, 1937.

[2] A. Devonshire, "Xcvi. theory of barium titanate," *Philosophical Magazine Series 7*, vol. 40, no. 309, pp. 1040–1063, 1949.

[3] A. Devonshire, "Cix. theory of barium titanate: Part ii," *Philosophical Magazine Series 7*, vol. 42, no. 333, pp. 1065–1079, 1951.

[4] V. Fridkin and S. Ducharme, *Ferroelectricity at the Nanoscale: Basics and Applications*. Heidelberg: Springer, 2014.

[5] W. Zhang and K. Bhattacharya, "A computational model of ferroelectric domains. Part I: model formulation and domain switching," *Acta Mater.*, vol. 53, no. 1, pp. 185–198, 2005.

[6] K.-C. Chen, W.-W. Wu, C.-N. Liao, L.-J. Chen, and K. N. Tu, "Observation of atomic diffusion at twin-modified grain boundaries in copper.," *Science*, vol. 321, pp. 1066–9, Aug. 2008.

[7] Y. Su and C. M. Landis, "Continuum thermodynamics of ferroelectric domain evolution: Theory, finite element implementation, and application to domain wall pinning," *Journal of the Mechanics and Physics of Solids*, vol. 55, no. 2, pp. 280–305, 2007.

[8] C. L. Kelchner, S. J. Plimpton, and J. C. Hamilton, "Dislocation nucleation and defect structure during surface indentation," *Phys. Rev. B*, vol. 58, pp. 11085–11088, 1998.

[9] N. Nadkarni, C. Daraio, R. Abeyaratne, and D. M. Kochmann, "Universal energy transport law for dissipative and diffusive phase transitions," *Physical Review B*, vol. 93, p. 104109, March 2016.

[10] S. Allen and J. Cahn, "Ground state structures in ordered binary alloys with second neighbor interactions," *Acta Metallurgica*, vol. 20, no. 3, pp. 423 – 433, 1972.

[11] S. M. Allen and J. W. Cahn, "A microscopic theory for antiphase boundary motion and its application to antiphase domain coarsening," *Acta Metallurgica*, vol. 27, pp. 1085–1095, June 1979.

[12] N. Nadkarni, A. F. Arrieta, C. Chong, D. M. Kochmann, and C. Daraio, "Unidirectional transition waves in bistable lattices," *Phys. Rev. Lett.*, vol. 116, p. 244501, Jun 2016.

[13] J. Raney, N. Nadkarni, C. Daraio, D. Kochmann, J. Lewis, and K. Bertoldi, "Countering dissipation by bistability: Stable propagation of mechanical signals in soft media," *Proc. Natl. Acad. Sci.*, 2016. In press.

[14] G. Noh and K.-J. Bathe, "An explicit time integration scheme for the analysis of wave propagations," *Computers & Structures*, vol. 129, pp. 178–193, August 2013.